OUKA
The University of Osaka
Institutional Knowledge Archive

Title	Design and construction of the cylindrical drift chamber for the COMET Phase-I experiment
Author(s)	Sato, A.; Yoshida, H.; Moritsu, M. et al.
Citation	Nuclear Instruments and Methods in Physics Research, Section A: Accelerators, Spectrometers, Detectors and Associated Equipment. 2024, 1069, p. 169926
Version Type	VoR
URL	https://hdl.handle.net/11094/98586
rights	This article is licensed under a Creative Commons Attribution-NonCommercial 4.0 International License.
Note	

The University of Osaka Institutional Knowledge Archive : OUKA

https://ir.library.osaka-u.ac.jp/

The University of Osaka

Nuclear Instruments and Methods in Physics Research A 1069 (2024) 169926

Contents lists available at ScienceDirect

Nuclear Inst. and Methods in Physics Research, A

journal homepage: www.elsevier.com/locate/nima

Full Length Article

Design and construction of the cylindrical drift chamber for the COMET Phase-I experiment

A. Sato [a,*], H. Yoshida [a,b], M. Moritsu [c,*], X. Jiang [d,e], Y. Kuno [a,b], H.-B. Li [d,e], W.-G. Li [d,e,1], Y. Matsuda [a], H. Miao [d,e], Y. Nakamura [a], Y. Nakatsugawa [g], Y. Nakazawa [h], S. Ohta [a], K. Okinaka [a], H. Sakamoto [a], M.L. Wong [a,2], T.S. Wong [a], C. Wu [d,f,*], T.-Y. Xing [d,e], T. Yamane [a], Y. Yuan [d,e], J. Zhang [d,e], Y. Zhang [d], Z.-K. Zhang [d,e]

[a] Department of Physics, Osaka University, 1-1 Machikaneyama, Toyonaka, 560-0043, Osaka, Japan
[b] Research Center for Nuclear Physics, Osaka University, 10-1 Mihogaoka, Suita, 567-0047, Osaka, Japan
[c] Department of Physics, Kyushu University, 744 Motooka, Nishi-ku, 819-0395, Fukuoka, Japan
[d] Institute of High Energy Physics, Chinese Academy of Sciences, 100049, Beijing, China
[e] University of Chinese Academy of Sciences, 100049, Beijing, China
[f] Spallation Neutron Source Science Center, 523808, Dongguan, China
[g] Wakayama Medical University, 811-1 Kimiidera, Wakayama, 641-8509, Wakayama, Japan
[h] KEK, 1-1 Oho, Tsukuba, 305-0801, Ibaraki, Japan

ARTICLE INFO

Keywords:
Gas detector
Drift chamber
Cylindrical detector
Muon
Particle physics
Lepton-flavor violation

ABSTRACT

COMET is an experiment at J-PARC that searches for the charged lepton flavor violating process of neutrinoless muon-to-electron conversion ($\mu \rightarrow e$ conversion) in a muonic atom. The COMET Phase-I experiment, which represents the first stage of its staged approach, utilizes the cylindrical drift chamber (CDC) as the main detector to measure the momentum of electrons emitted from $\mu \rightarrow e$ conversion in a 1 T magnetic field. The CDC is designed for optimal performance to achieve the best momentum resolution and effectively separate the $\mu \rightarrow e$ conversion electron signal from background signals. This design entails adapting He:i-C_4H_{10} (90:10) as its chamber gas and employing an all-stereo wire configuration. This document provides a comprehensive overview of the CDC detector, encompassing design considerations, mechanical structure, construction methodologies, and results of performance evaluations conducted using cosmic-rays.

1. Introduction

The COMET experiment is a dedicated search for charged lepton flavor violation (CLFV) in muonic atoms, with a specific focus on the process of neutrinoless muon to electron conversion ($\mu \rightarrow e$ conversion). This process is considered a promising avenue for discovering new physics beyond the Standard Model (BSM) [1]. The COMET Phase-I experiment [2] is the first stage in a staged approach, aiming to achieve a factor of 100 improvement over the current upper limit of $\mu \rightarrow e$ conversion, which is $\lesssim 7\times10^{-13}$ 90% C.L. for a gold target [3]. The high sensitivity of the COMET Phase-I experiment could potentially probe new physics models up to energy scales of O(10^4) TeV, surpassing the capabilities of collider experiments. Thus, CLFV research complements searches for BSM at the Large Hadron Collider (LHC).

Fig. 1 shows the schematic layout of the COMET Phase-I experiment, which consists of a series of superconducting solenoid magnets; the pion capture solenoid (CS), the muon transport solenoid (TS), and the detector solenoid (DS). Pions and muons are produced by injecting a 8 GeV proton beam into the pion production target located in CS. These charged particles are then captured by the 5 T solenoidal magnetic field in CS and guided through TS to DS, where the muons are stopped in the muon stopping target made of thin aluminum disks. Within the warm bore of DS, which generates a 1 T magnetic field, the cylindrical detector system (CyDet) is located. CyDet comprises a cylindrical drift chamber (CDC) and trigger hodoscopes, as depicted in Fig. 2.

The CDC plays a crucial role in the COMET Phase-I experiment by providing primary momentum measurement for electrons from $\mu \rightarrow$

* Corresponding authors.
E-mail addresses: sato@phys.sci.osaka-u.ac.jp (A. Sato), moritsu.manabu@phys.kyushu-u.ac.jp (M. Moritsu), wuchen@ihep.ac.cn (C. Wu).
[1] Deceased 19 June 2023.
[2] Present address: Department of Physics, University of Liverpool, Liverpool, L69 3BX, UK.

https://doi.org/10.1016/j.nima.2024.169926
Received 28 May 2024; Received in revised form 2 September 2024; Accepted 24 September 2024
Available online 30 September 2024
0168-9002/© 2024 The Authors. Published by Elsevier B.V. This is an open access article under the CC BY-NC license (http://creativecommons.org/licenses/by-nc/4.0/).

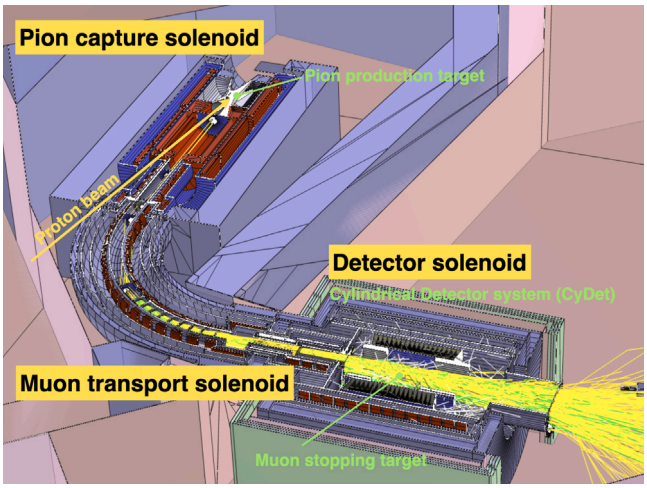

Fig. 1. Cutaway view of the Phase-I layout of the COMET experiment, showing the pion capture solenoid, the muon transport solenoid composed of the 90 degree bend which removes wrong-sign particles as well as selecting the momentum of the particles which travel through to the detector solenoid in the foreground.

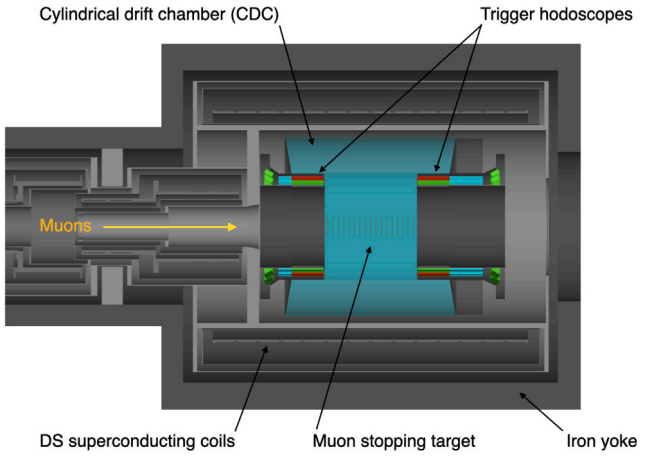

Fig. 2. Schematic layout of the CyDet detector.

e conversion. It efficiently identifies and measures 104.9 MeV/c signal electrons while effectively rejecting backgrounds. To achieve this, we have adopted the CDC, which features a large inner radius and surrounds the muon stopping target, for tracking charged particles. This approach ensures that most beam particles, which do not stop in the muon stopping target, proceed downstream and exit the detector region without leaving any hits in the detector system. Consequently, both the background event rate and the background hit rate in the CyDet detector are reduced. A notable feature of the COMET Phase-I experiment is the use of a pulsed beam. This feature enables only the tracks that arrive after the beam pulse to be measured, effectively eliminating the prompt beam backgrounds. Therefore, any detector system, such as the CDC, should be able to withstand the large flux of charged particles during the burst of "beam flash" particles. The time window for the measurement of electrons from $\mu \rightarrow e$ conversion in COMET will start several hundred nanoseconds after the prompt flash with a beam repetition of 1.17 μs.

This paper focuses on the design and construction of the CDC, organized as follows: Section 2 discusses the overarching design considerations. The mechanical structure of the chamber is outlined in Section 3, followed by a detailed description of its construction in Section 4. The readout electronics is presented in Section 5. Results with

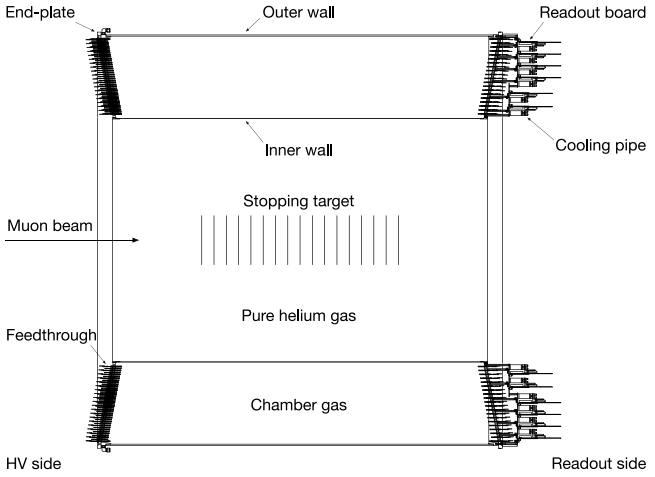

Fig. 3. Schematic layout of the CDC.

cosmic-ray tests are reported in Section 6. The operational environment of the CDC in the COMET Phase-I is described in Section 7. The paper concludes with a brief summary in Section 8.

2. Design considerations

The CDC is a crucial component of the COMET Phase-I experiment, which reconstructs tracks of charged particles in the solenoid magnetic field and measures their momenta precisely. It is designed to avoid high hit rates due to beam particles, electrons from muon decays in orbit (DIO) in muonic atoms, and low-energy protons emitted from excited nuclei produced by the muon nuclear capture process. Among the small fraction of particles that eventually enter the CDC and leave hits, DIO electrons and low-energy protons dominate. However, the hits from protons can be easily identified using the energy deposit in the CDC cells because their energy loss is about 100 times larger than that of a signal electron.

The layout of the CDC is shown in Fig. 3, and its main parameters are summarized in Table 1. The length of the CDC at the inner and outer walls is 1495.5 mm and 1577.3 mm, respectively. The radii of the inner and outer walls are determined to avoid DIO electrons with momentum less than 60 MeV/c from hitting the CDC and to fully cover the tracks of 104.9 MeV/c signal electrons. The inner wall of the CDC is made of 0.5 mm thick carbon fiber reinforced plastic (CFRP), while the outer wall is made of CFRP of 5 mm thickness. The inner and outer walls have thin aluminum foils glued inside to eliminate charge-up on the CFRP. The end-plates are conical in shape, and the thickness of the end-plate is about 10 mm to rigidly support feedthroughs. Trigger hodoscopes are placed at both the upstream and downstream ends of the CDC.

The inner volume of the inner wall is filled with pure helium gas. The pressure of this helium gas is set slightly higher than that of the chamber gas in the CDC. This allows the use of the thin inner wall and also reduces multiple scattering before entering the CDC.

The momentum resolution of the CDC must be about 200 keV/c for the 104.9 MeV/c electrons to achieve the target sensitivity of COMET Phase-I. Based on the CDC design a Monte Carlo simulation has been conducted. A typical track for a signal event is shown in Fig. 4. The signal electron generated in the stopping target enters the CDC with a helical motion in the magnetic field and finally hits a trigger hodoscope, producing a trigger signal. The electron momentum is reconstructed using the Genfit track fitting package [4]. Fig. 5 shows the momentum distributions for the reconstructed $\mu \rightarrow e$ conversion signals and reconstructed background DIO events for the case of momentum resolution of 200 keV/c. The vertical scale is normalized such that the integral of the signal curve equals to one event. This assumes a conversion rate of

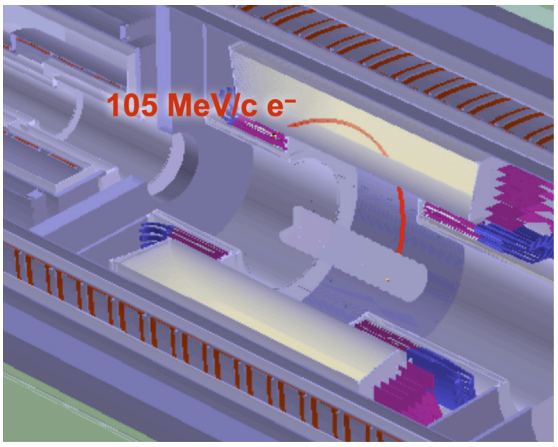

Fig. 4. Typical track in the CyDet detector for a simulated signal electron with 105 MeV/c.

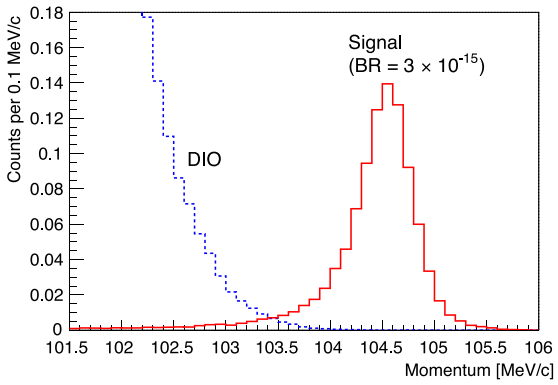

Fig. 5. Expected reconstructed momentum distribution for signal electrons (solid line) and decay-in-orbit (DIO) events (dashed line), under the assumption of the signal branching ratio of 3×10^{-15} and the momentum resolution of 200 keV/c.

$\mathrm{BR}(\mu^- + Al \to e^- + Al) = 3.1 \times 10^{-15}$. Since the intrinsic momentum resolution in such a low-energy region is dominated by multiple scattering effects, the CDC must be a low-mass detector. These requirements lead to choices in cell configuration, wires, and gas mixture.

2.1. Layer configuration

The CDC is arranged in 20 concentric sense wire layers including 2 guard layers with alternating positive and negative stereo angles. The positions of the wires on the readout side end-plate are shown in Fig. 6. The 1st and 20th sense wire layers operate at a lower high voltage (HV) and act as guard layers. Their function is to remove the space charge that accumulates due to ionization created in the regions between the inner (or outer) walls and the guard layer. Without these layers, space charge would accumulate in the absence of an electric field.

2.2. Cell configuration

Each cell in the CDC has one sense wire surrounded by an almost-square grid of field wires. The ratio of the total numbers of field to sense wires is 3:1, and the cell size is nearly constant over the entire CDC region, such as 16.8 mm wide and 16.0 mm high. In a strict sense, the cell width does indeed vary slightly from layer to layer. Additionally, the cell height changes along the longitudinal direction due to stereo drops and gravitational effects. Moreover, the cell shape deviates from a perfect rectangle because of the alternating stereo wire structure, as illustrated in Fig. 6. Square cells are well-suited to low momentum tracks (such as those from the $\mu \to e$ conversion signal), which might enter the drift cells with large angles with respect to the radial direction. The stereo angle is set to 64–75 mrad, which is selected to achieve a longitudinal spatial resolution of about 3 mm. With this design, where all wires are set at stereo angles, the shape of each layer's

Table 1
Design parameters of the CDC.

Inner wall	Material	CFRP, Al
	Length	1495.5 mm
	Radius	495.95–496.5 mm
	Thickness	CFRP: 0.5 mm, Al: 0.05 mm
Outer wall	Material	CFRP, Al
	Length	1577.3 mm
	Radius	829.9–835.0 mm
	Thickness	CFRP: 5.0 mm, Al: 0.1 mm
Number of sense layers		20 (including 2 guard layers)
Sense wire	Material	Au-plated W
	Diameter	25 μm
	Number of wires	4986
	Tension	50 g
	Stereo angle	±(64–75) mrad
Field wire	Material	Al alloy (A5056)
	Diameter	126 μm
	Number of wires	14 562
	Tension	80 g
	Stereo angle	±(64–75) mrad
Gas	Mixture	He:i-C_4H_{10} (90:10)
	Volume	2084 L

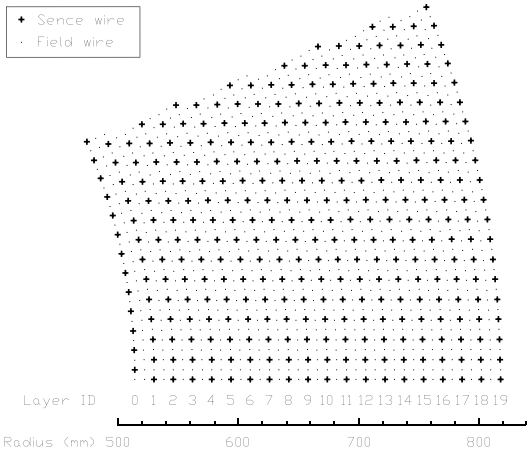

Fig. 6. Layout of wires in the CDC. Wire positions on the readout side end-plate are shown for one-eighth of the total area.

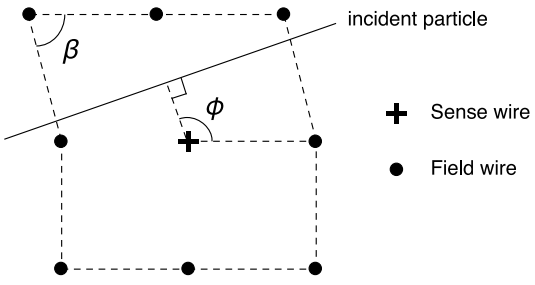

Fig. 7. Illustration of the shape of a cell consisting of one sense wire surrounded by eight field wires. As the position of the cell shifts relative to the CDC axis direction, the upper corner angle β changes periodically. The relationship between time and space within the cell is determined by considering the periodicity of this β angle and the angle of incidence ϕ of the charged particle on the cell.

cell changes periodically as its position relative to the CDC axis shifts, similar to the design of the KLOE drift chamber [5]. Fig. 7 illustrates the shape of a cell at a specific radial position. The lower part of the figure corresponds to the inside of the CDC. In the COMET CDC, the wire layer containing the sense wire and its adjacent lower field wire layer have approximately the same stereo angle. The layer of field wires in the upper part of the cell belongs to the next outward cell and is set at an opposite stereo angle. As the position of the cell relative to the CDC axis changes, the relative positions of the wires in the lower two layers and the upper layer of the cell also shift, resulting in a variation in the cell's upper corner angle β.

The CDC has 4,986 sense wires and 14,562 field wires. The field wires are the most massive material in the CDC tracking volume. To reduce multiple scattering at the field wires, uncoated aluminum alloy (A5056) is adopted as the material for the field wires because of its low-Z and low density properties. Wire creeping in the A5056 alloy, which could potentially lead to a loss of tension over time, was tested in [6], and no issues were found in actual use. The intrinsic momentum resolutions of the CDC were estimated for two cases of field wire size: ø80 μm and ø126 μm. The ø80 μm wire shows better resolution than ø126 μm wire. The diameter of the field wire was determined by considering the maximum voltage that can be applied to the sense wires, the detection efficiency as well as the momentum resolution. To prevent degradation of the field wire surface, it is important to set the electric field on the field wire at 20 kV/cm or less to suppress the generation of whisker growth and corona discharges [7]. Electric field in the cell and the electric field strength at the field wire surface were calculated using the Garfield program [8] as shown in Fig. 8. We found that if the ø80 μm aluminum wire is used as the field wire, the operating voltage should be below +1730 V to keep the electric field on the wire surface below 20 kV/cm, while +1900 V can be applied with a surface electric field of only 14 kV/cm for field wires of ϕ126 μm. However, according to past tests with CDC prototypes [9], +1730 V is not enough to obtain a reasonable signal gain for the proposed gas mixture discussed below. Also we found that the difference in momentum resolution between ø80 μm and ø126 μm wire configurations does not significantly affect the physics sensitivity. Therefore, we decided to use the ø126 μm aluminum wire as the field wire. A tension of 80 g is applied to the field wires to match the gravitational sag of the sense wires.

The sense wires, made of gold-plated tungsten, have a diameter of 25 μm and are tensioned to 50 g. We selected 99.95% pure tungsten without a rhenium alloy due to its low electrical resistivity and cost-effectiveness. The deflection due to gravity is approximately 55 μm at the center of the CDC. The maximum difference in gravitational sag between the sense wires and the field wires is less than 100 μm. The total tension force exerted by all the wires amounts to 1.4×10^3 kg.

2.3. Gas mixture

The baseline choice of the gas mixture is He:i-C_4H_{10} (90:10), chosen to minimize multiple scattering, which dominates the deterioration of momentum resolution. This gas mixture adds little to the material budget, provides good position and energy-loss resolutions, and suppresses photon interactions due to its small cross section to photons. The radiation length of the He:i-C_4H_{10} (90:10) gas mixture is about 1400 m. In addition to that, the field and sense wires reduce the average value of the radiation length of the CDC tracking volume to 500 m. The He:i-C_4H_{10} (90:10) gas mixture has been utilized in drift chambers in the KLOE [5] and MEG-II [10,11] experiments. We have demonstrated through a prototype chamber test [9] that the design and gas mixture are suitable for the COMET CDC.

The drift velocity has also been calculated for different He:i-C_4H_{10} gas mixtures for comparison as shown in Fig. 9. For He:i-C_4H_{10} (90:10), typical drift lines for a cell are shown in Fig. 10. The magnetic field is roughly aligned with the wire direction, and therefore almost perpendicular to the electric field. The Lorentz angle (angle of deflection

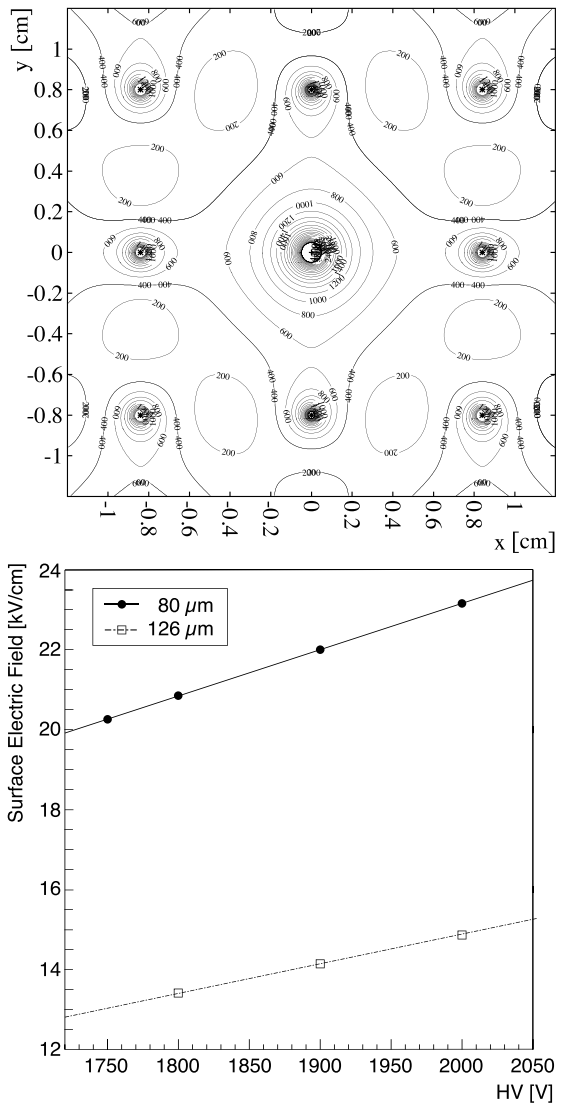

Fig. 8. Top: Contours of electric field distribution calculated by `Garfield` for a cell with sense and field wires of ø25 and ø126 μm, and HV of +1825 V. Bottom: Electric field at surface of the field wires as a function of applied high voltage for the field wire of ø80 μm and ø126 μm.

of the drift electrons with respect to the electric field in the presence of a crossed magnetic field) is much smaller than argon based gas mixtures [12]. The time–distance relationship is calculated as shown in Fig. 11. At high voltage of approximately +1800 – +1900 V is applied to the sense wires with the field wires at ground potential, resulting in an avalanche gain of approximately (1–4) $\times 10^4$ for the gas mixture of He:i-C_4H_{10} (90:10). The main properties of the chamber gas mixture used in the CDC is summarized in Table 2.

The gas system for the CDC utilizes separate pure gas bottles located in a gas stock booth outside. Gas mixing is carried out using two mass flow controllers. Each gas component has multiple connected gas bottles linked to pressure regulators, with exhaust ports equipped with diaphragm valves to prevent air contamination during bottle replacement. Only the CDC detector and a buffer tank with a pressure gauge are situated in the underground experimental room, while other gas equipment and devices are located on the ground floor to mitigate radiation damage to the electronics. Gas is delivered to the detector through a metal gas pipe. The gas system comprises a circulation pump, flow controllers, pressure controllers, oxygen filters and monitors, humidity monitors, and buffer tanks in the circulation line, as depicted in Fig. 12.

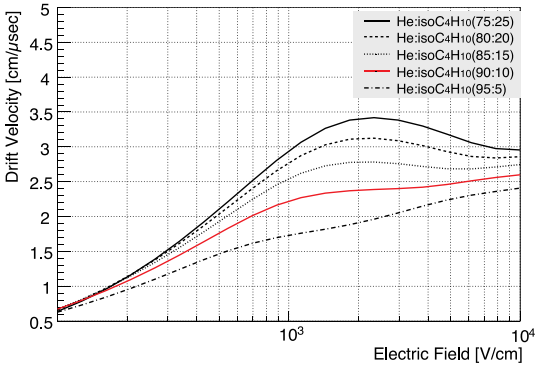

Fig. 9. Drift velocity in different gas mixtures of He:i-C_4H_{10} as a function of the electric field strength, calculated by `Garfield`.

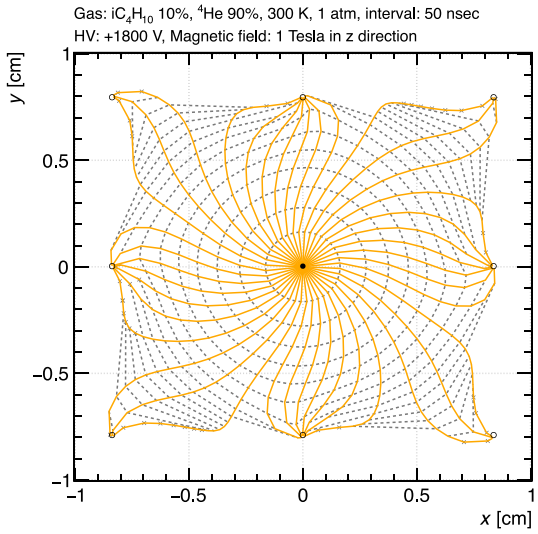

Fig. 10. Typical single cell layout with drift lines and isochrones of 50-ns intervals at 1 T magnetic field to the z direction with a gas mixture of He:i-C_4H_{10} (90:10) with a voltage of +1800 V.

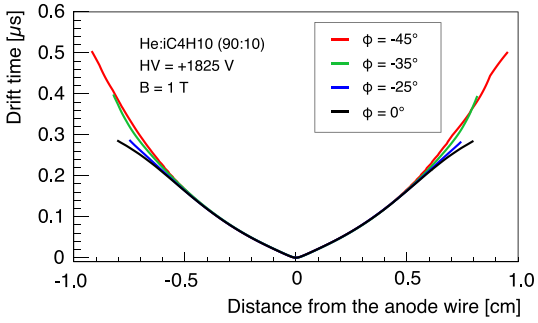

Fig. 11. Example of the time to space relationship with different incident angles (ϕ) for He:i-C_4H_{10} (90:10) with a high voltage of +1825 V and a 1 Tesla magnetic field. The corner angle β is set to 0.

To efficiently remove oxygen from the CDC gas volume, a certain flow rate (e.g., approximately 2 L/min) is required. An oil-free metal bellows pump circulates the gas, with a small amount of hydrogen mixed into the oxygen filter as a Platinum catalyst. Fresh gas is fed in at only 1/10 of the circulation flow rate to reduce consumption, with the exhaust flow rate matching the feeding rate. Pressure in the CDC is regulated by a mass flow controller, with feedback from the pressure gauge on the buffer tank connected to the CDC output, always maintained

Table 2
The main properties of the chamber gas mixture used in the CDC at 20 °C and 1 atm.

Parameter	Value
Gas mixture	He:i-C_4H_{10} (90:10)
Pressure	1 atm
Density	4.0×10^{-4} g/cm^3 [13]
Radiation length	1400 m [13]
Mean energy to generate one electron–ion pair	39 eV [14]
No. of primary electron–ion pairs*	12.7 cm^{-1} [12]
No. of total electron–ion pairs*	26.7 cm^{-1} [12]
Drift velocity for E = 0.6–2.0 kV/cm	1.8–2.4 cm/μs

* Values for minimum ionizing particles.

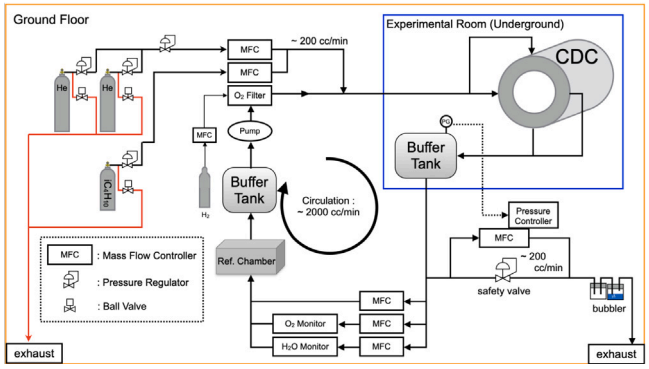

Fig. 12. Schematic view of the gas system for the CDC.

slightly higher than atmospheric pressure (e.g., 1050 hPa). Pressure within the CDC volume should be controlled within approximately 1% accuracy for optimal performance, although gain fluctuations can be compensated for in offline analysis. Output gas is directed to the air exhaust port in the experimental hall. Input flow rates into the oxygen and humidity monitors are controlled by two mass flow controllers to accurately measure oxygen and humidity levels. Oxygen concentration should ideally be below 50 ppm with the oxygen filter, while water concentration is adjustable around 500–1200 ppm to suppress the Malter effect. The buffer tanks are installed to mitigate drastic pressure changes, each with a volume of about 100 L.

For safety and stability, most devices should be monitored and controlled remotely. Additionally, it is necessary to install a heating system or position the bottle on the ground floor, where the room temperature is sufficiently high, to prevent i-C_4H_{10} from liquefying inside the gas transfer tubes.

3. Mechanical structure

The CDC consists of three principal mechanical components: the end-plates, the inner wall, and the outer wall. In the design phase for the end-plates, two configurations were considered: a flat plate design and a cone-shaped plate design. The latter was selected for its ability to withstand the wire tension load. The construction materials chosen were 0.5 mm-thick carbon-fiber reinforced plastic (CFRP) for the inner wall and 5 mm-thick CFRP for the outer wall. Initially, the inclusion of a proton absorber in front of the CDC's inner wall was planned to reduce proton infiltration from muon capture in the stopping target. However, subsequent analysis of the proton emission rate following muon capture in aluminum indicated that the proton yield with momenta above 60 MeV/c is sufficiently low [15,16], eliminating the need for the proton absorber.

3.1. Mechanical strength study

The mechanical strength has been calculated using the SolidWorks (Premium 2013 x64 Edition) CAD program, which incorporates a Finite

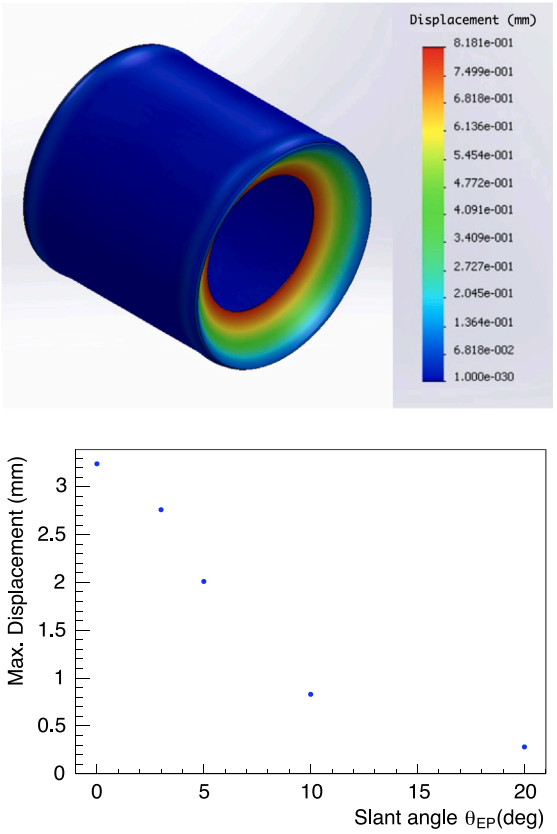

Fig. 13. Results of SolidWorks simulation of the mechanical deformations in the end-plates and the outer wall of the CDC for the total wire tension load of 1.4×10^3 kg. The top figure is an example of a calculation result showing the amount of displacement in three dimensions for the case of the slant angle θ_{EP}=10 degrees. The bottom figure shows maximum displacement as a function of the slant angle of the cone-shaped end-plate.

Element Analysis function. The total wire tension load is calculated to be 1.4×10^3 kg based on the parameters described in Table 1. The end-plates are designed with a conical shape, incorporating a slight slant angle so that the distance between the end-plates gradually decreases toward the center of the CDC. This slant angle, denoted as θ_{EP}, was varied within the range of 0 to 20 degrees to assess the stress and deformation on the end-plates and the outer wall of the CDC, as illustrated in Fig. 13. It is noted that no CDC inner wall was installed in the setup of this study strength due to its insufficient thickness to support the wire load. For this case, the maximum deformation of the end-plate is estimated to be 0.83 mm with θ_{EP}=10 degrees. This meets our requirements.

3.2. Feedthrough

The COMET CDC utilizes feedthroughs to securely anchor wires while insulating the high voltage from the end-plate ground. Fig. 14 illustrates the feedthrough's dimensions. Adopted from the design used in the Belle-II CDC [17], the feedthrough in the COMET CDC features a body insulator made from Noryl, chosen for its excellent high-voltage insulation properties. The feedthrough pins are crafted from aluminum, selected to maintain wire tension for the field wires. These pins are also electrically connected to the aluminum end-plates via additional cables. All the sense and field wires are secured to these pins by crimping, and the wire position is fixed at the bushing within the hole diameters of 80 μm and 200 μm for the sense and field wires, respectively.

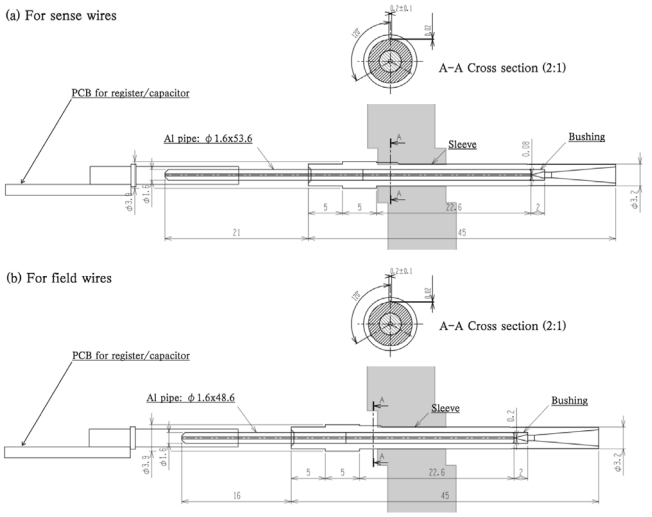

Fig. 14. Feedthrough for the COMET CDC. (a) is for sense wires, and (b) is for field wires.

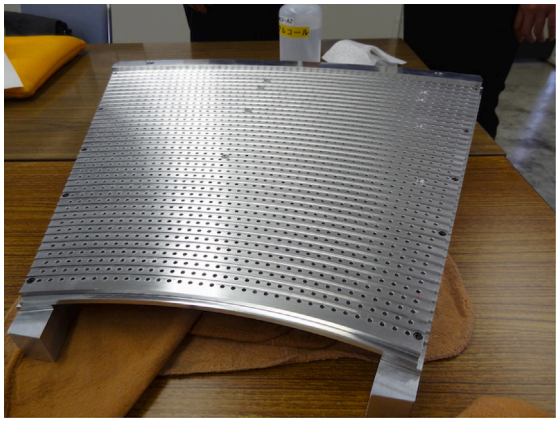

Fig. 15. Picture of a prototype of 1/12 size end-plate.

4. Construction

The construction of the CDC began once the comprehensive design was established. This process started with the production of two aluminum end-plates. Simultaneously, the outer CFRP (Carbon Fiber Reinforced Plastics) wall was being fabricated. Following the assembly of these end-plates and the outer wall, they were then transported to a clean room designated for wire stringing.

The wire stringing phase, including all necessary preparation and cleaning, took approximately six months to complete. Concurrently, the inner CFRP wall was being fabricated and was later installed into the CDC. This installation occurred only after the completion of wire stringing and once the tension of each wire was meticulously verified.

This section methodically outlines each step involved in the CDC's construction process.

4.1. Construction of end-plates and outer wall assembly

Before construction began, a prototype of 1/12 of the end-plate was constructed to examine the accuracy of hole positions using a computer-controlled drilling machine. Fig. 15 shows a picture of the prototype end-plate. The prototype contains a total of 1668 holes with a nominal diameter of 3.2 mm.

A 3D camera device (NEXIV VMR-10080) was used to measure the geometry of the prototype end-plate. The accuracy of machining

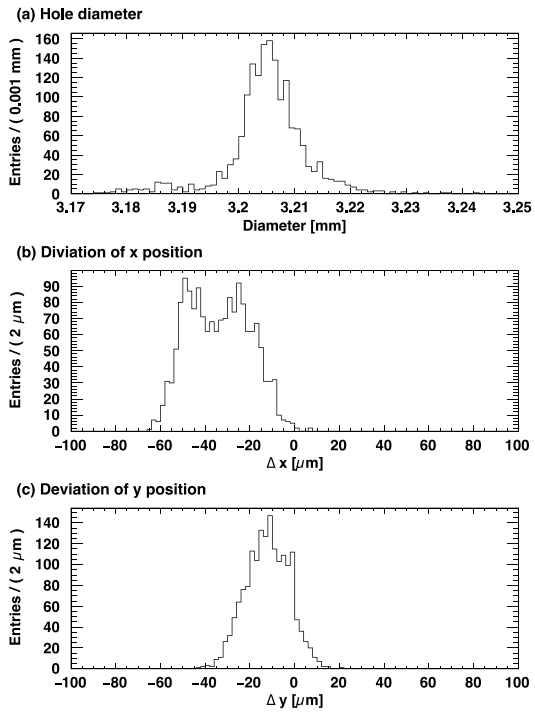

Fig. 16. Distributions of the measured geometry of feedthrough holes on the prototype end-plate: (a) hole diameter, (b) deviation of the x position, and (c) deviation of the y position from the design values.

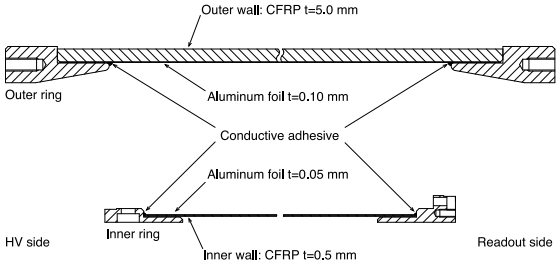

Fig. 17. Longitudinal cross-section drawing of the CDC, illustrating both the outer and inner walls along with the support rings.

was checked by calculating the diameter and center position of all feedthrough holes which were automatically detected based on 4 points on the edges of the holes. Fig. 16 shows the distributions of the measured values. The drilling machine design precisions are 0.01 mm in diameter and 0.05 mm in positions. The diameter of the hole should be adequate to hold the feedthrough and prevent gas leakage. Several holes displayed small diameters, but it was found that this was due to burrs created during drilling. We confirmed that the feedthroughs fit the holes without any problem. Despite slight offsets in the x and y positions, the dispersions are consistent with the machine precision. These offsets in x and y coordinates were corrected before the actual end-plate construction.

The outer wall is constructed from CFRP, measuring 5 mm in thickness, and has 100-μm thick aluminum films adhered to the inside. The support rings were affixed to both edges of the wall using conductive epoxy adhesive, ensuring the aluminum films were electrically connected to the rings. Fig. 17 provides a schematic representation of the walls and support rings. The end-plates and the outer wall were joined using bolts with epoxy adhesive and subsequently transported to a clean room for wire stringing.

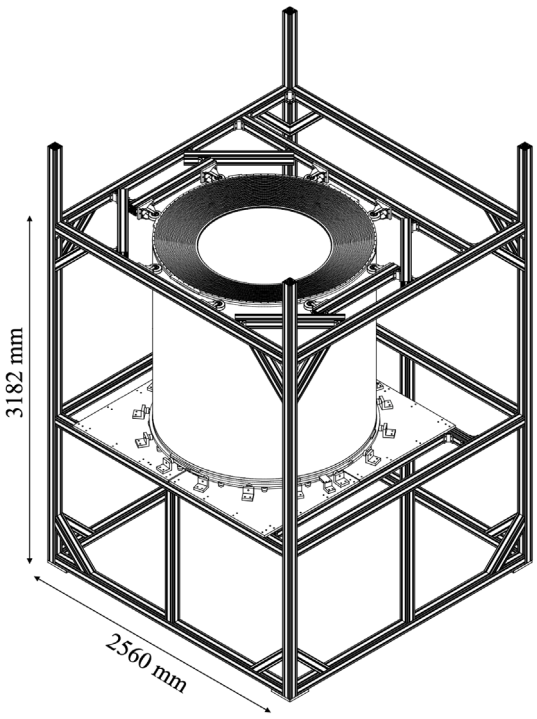

Fig. 18. Sketch of the CDC wire stringing cradle.

4.2. Wire stringing and tension measurements

For the wire stringing process, the CDC was vertically mounted on a specially designed cradle, as shown in Fig. 18. The cradle was equipped with ball bearings, allowing the end-plates to rotate smoothly. This setup enabled the systematic progression of wire stringing from the outer to the inner layer. To avoid entanglement of the stringing wire with previously strung wires in the outer layers, the cradle was strategically tilted. The wires were strung one by one by hand, with the assistance of support equipment. Using an automated wire reel system, each wire was fed from the upper to the lower side, aided by a weight to ensure proper tension before being clamped to the feedthrough pin.

Before initiating the wire stringing process, a pre-load tension of approximately 1400 kg was applied between the two end-plates to counterbalance the anticipated wire tension load. To achieve this, 12 aluminum tension bars equipped with springs and bolts were installed, with a dial gauge used to precisely measure the displacement between the end-plates. After applying the 1400 kg load, the observed displacement matched the pre-calculated value of 1 mm, confirming the accuracy of the setup.

The tension of the strung wires was assessed at the end of each working day, immediately following the stringing activities. The tension force T of a wire can be derived from its measured resonant frequency f using the formula:

$$f = \frac{1}{2L}\sqrt{\frac{T}{\rho}}, \tag{1}$$

where L represents the effective length of the wire, and ρ denotes the wire's linear density. To measure the resonant frequency, a permanent magnet and an alternating current (AC) source were connected to the wire, inducing wire oscillations through the Lorentz force generated by the magnetic field and the AC. The resonant frequency was determined by varying the frequency of the AC. A specialized module was employed to ascertain the resonant frequency, thereby measuring the wire tension. Should the measured tension deviate by more than 10%

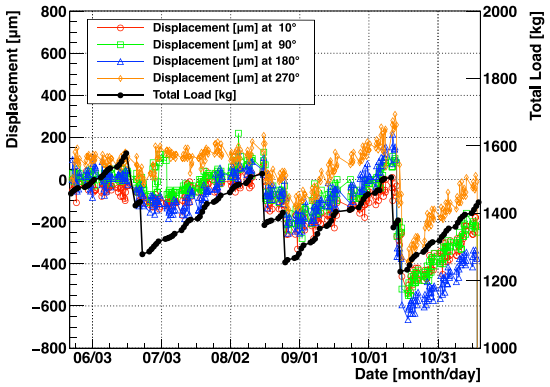

Fig. 19. Transition of displacements between the two end-plates, monitored at four distinct points, alongside the cumulative load exerted by the strung wires and tension bars.

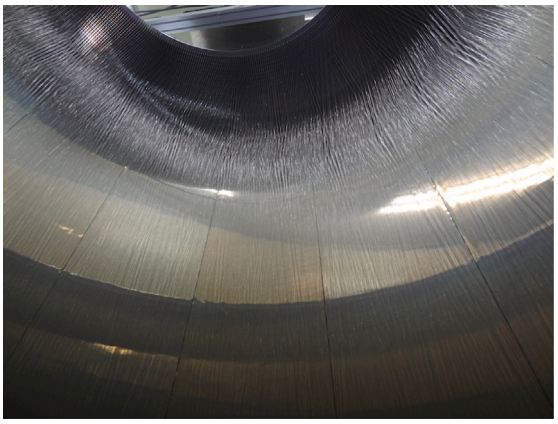

Fig. 20. Photograph of the interior of the CDC after the wire stringing was completed.

from the preset values (50 g for the sense wires and 80 g for the field wires) the wire in question was deemed unsatisfactory, removed, and re-strung. This meticulous approach ensures that all wires meet the stringent design specifications for optimal performance.

In addition to wire tension, the displacement between the two end-plates was meticulously monitored. This was accomplished using four dial gauges, with readings taken three times daily. A direct correlation was observed between the displacements and the total load exerted by the strung wires and tension bars, as shown in Fig. 19. To mitigate the load from the tension bars, adjustments were made either by reducing the spring load or by sequentially removing the tension bars. Overall, six load alleviation steps were carried out, culminating in the removal of all tension bars by the end of the process. The wire stringing phase spanned 121 working days, culminating in the successful assembly of the CDC. A photograph capturing the interior of the CDC after the completion of wire stringing is shown in Fig. 20.

Here, we explain the procedure for replacing a defective wire. Replacing field wires is notably simpler than replacing sense wires, primarily due to the greater stretchability of the aluminum wire used for field wires. The field wire can be manually extended, allowing a fishing line to be attached to its end. This setup makes it easy to pull out the defective field wire along with the attached fishing line. A new field wire can then be threaded through using the fishing line, even within the complex stereo layer structure. In contrast, replacing sense wires is more challenging. The process begins with the complete removal of the defective sense wire. To facilitate this, an adjacent field wire is selected as a temporary replacement (sacrifice), which is then exchanged with a fishing line. The fishing line serves a dual purpose: it allows for the replacement of both the sense wire and the sacrificed field wire. The sequential steps involved in this replacement process are depicted in Fig. 21.

4.3. Wire tension and gravitational sag

Following the completion of the wire stringing process, the tension of all 19,548 wires was meticulously rechecked to account for any potential changes in the distance between the two end-plates. The measured tension and the positioning of both sense and field wires are detailed in Fig. 22. This comprehensive reevaluation uncovered a significant tension reduction in the aluminum field wires within the inner layers, showing a decrease of approximately 20 g from the initial measurements. The removal of the innermost tension bars, and consequently, the absence of tension bars, was observed to contribute to a decreased distance between the two end-plates. This reduction was attributed to the cumulative tension exerted by the inner wires. As a result, the shorter distance between the end-plates led to the observed drop in wire tension.

Wire tension is a critical factor in determining gravitational wire sag when the chamber is oriented horizontally. The gravitational sag, d, at the center of a wire is calculated as described in [18]:

$$d = \frac{\rho L^2}{8T}. \tag{2}$$

One may notice that the maximum sagged position slightly deviates from the center of the wire in case of stereo wires; we ignored it here because of our small stereo angles. Electrostatic force on the sagged wire is also discussed in [18]. We found that the wire is stable against the electrostatic force whereas the sag increases by around 4%–5% based on an approximate coaxial-tube calculation; therefore it is also ignored here.

Fig. 23 shows gravitational sags for the sense wires calculated from the measured tension. A nominal sense wire tension of 50 g results in a sag of 55 μm. Sense wires exhibiting a sag greater than 70 μm were identified and replaced, ensuring that the gravitational sag for sense wires is maintained within a controlled range of 48 to 61 μm. It is noteworthy that this calculated sag will be considered in tracking analysis.

For field wires, the emphasis is on the relative difference in wire sags between a sense wire and its surrounding field wires to prevent cell shape deformation. With a nominal field wire tension of 80 g correlating to a sag of 120 μm, the expected sag difference from a sense wire is 65 μm. Fig. 24 displays the calculated sag differences between sense wires and adjacent field wires within each cell. Considering the uniform stereo angle in the inner layer relative to a sense wire, the analysis focused on neighboring field wires on both sides within the same layer, and on three field wires in the inner layer that form the drift cell with the sense wire. The figure's zigzag pattern reflects the process of tension-bar alleviation mentioned previously. To maintain sag differences from a sense wire below 100 μm, several tens of field wires exhibiting sags larger than 170 μm were replaced. This careful management of wire sag differences ensures that cell shape deformation does not significantly distort the electric field.

4.4. Inner wall installation and leak test

The inner wall of the CDC, constructed from 0.5-mm thick CFRP, is depicted in Fig. 17. To achieve electrical grounding, thirteen pieces of 50-μm thick aluminum film were adhered to the outer surface of the wall. The dimensions of the support rings were precisely adjusted following the inner wall's fabrication to ensure a perfect fit. The assembly of the inner wall was meticulously installed into the CDC using special guide rails. This process required exceptional precision due to the minimal gap of only 250 μm between the end-plate and the ring. To guarantee gas tightness, the joints were sealed with RTV silicone rubbers KE45-T made by Shin-Etsu Silicone.

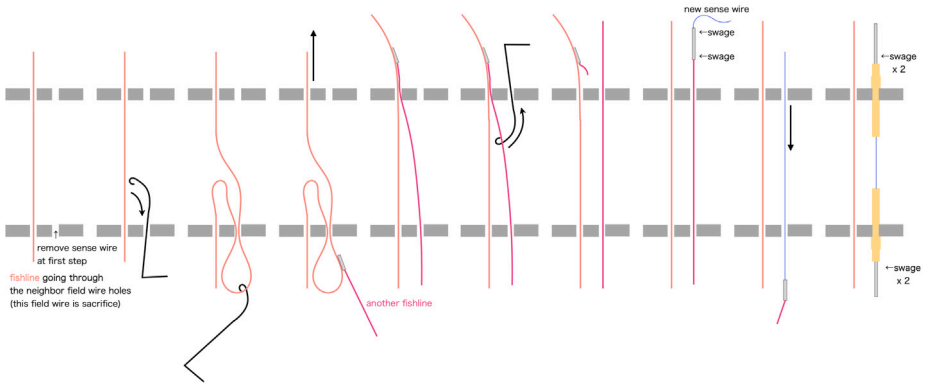

Fig. 21. Step-by-step procedure for replacing a sense wire, with the sequence of actions progressing from left to right.

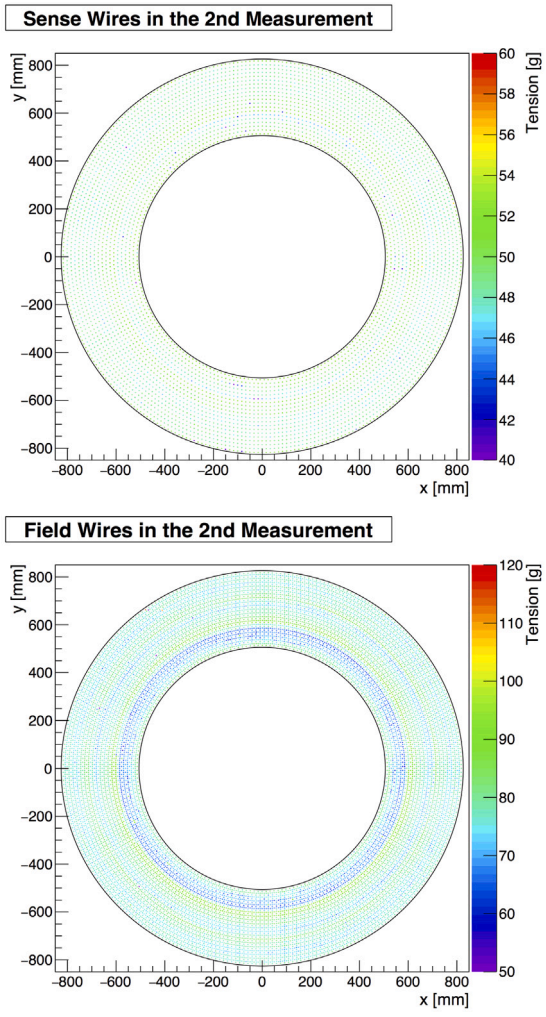

Fig. 22. Detailed view of the tension and positions of wires within the CDC, as observed from the downstream side. The top section displays the sense wires, while the bottom section focuses on the field wires. Upon reviewing the tensions, several wires that did not meet our specified tension criteria were identified and subsequently replaced.

Following the installation of the inner wall, the CDC underwent horizontal mounting on a cradle for gas tightness testing using helium gas. The leak rate was determined to be less than 20 cc/min, equivalent to less than 1% of the gas circulation flow rate of our system. This leak rate is deemed sufficiently low to maintain optimal gas quality within the chamber during its operational use.

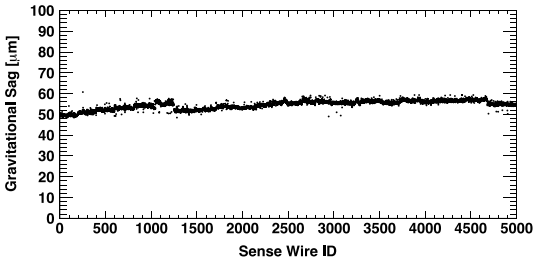

Fig. 23. Gravitational wire sag at the center of the sense wires.

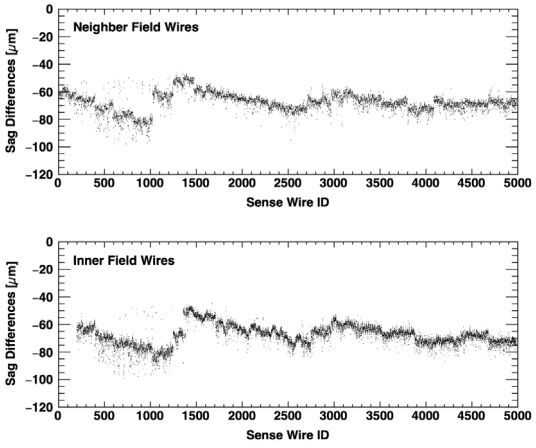

Fig. 24. Differences of the gravitational wire sag between a sense wire and surrounding field wires in each cell. The upper plot is for neighbor field wires in the same layer of the sense wire. The lower plot is for three field wires in the inner layer of the sense wire.

5. Readout system

In order to record the charge and timing information from the hit wires, we have adopted the electronic circuit board initially developed for the Central Drift Chamber of the Belle-II experiment [17,19] as the readout board for the COMET CDC. This board is referred to as RECBE [20,21]. Each board processes analog signals from 48 sense wires. The amplified analog signals are digitized to capture arrival time and waveform information. Data calculated by a built-in Field Programmable Gate Array (FPGA), such as the integral charge, are transferred to a backend data-acquisition system via Ethernet upon receiving a trigger input.

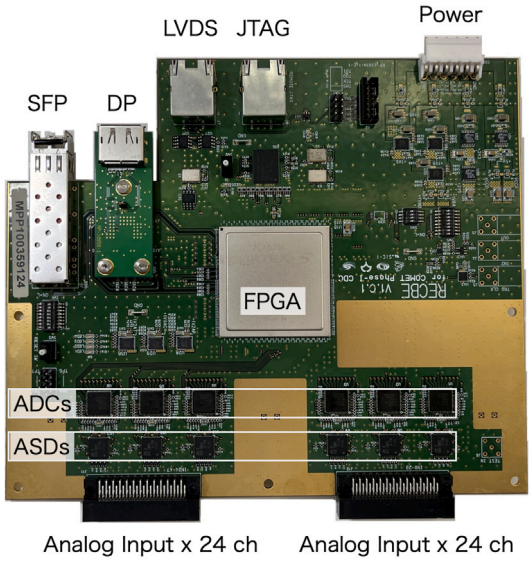

Fig. 25. The COMET CDC front-end readout board.

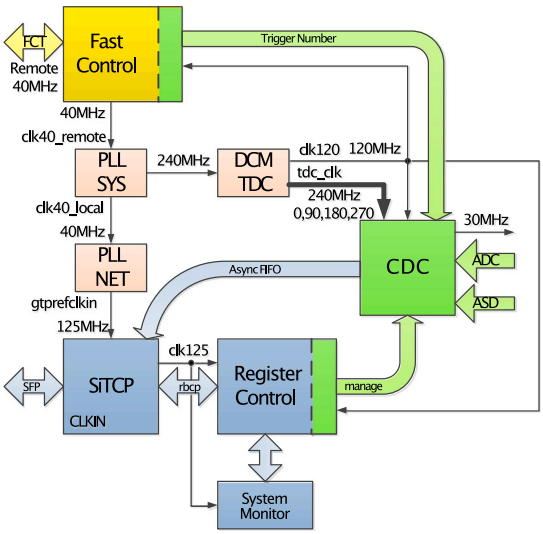

Fig. 26. Block diagram of the RECBE firmware.

5.1. Readout board and firmware

Fig. 25 shows a photograph of the readout board built for the COMET CDC. It features two connectors, each capable of accepting a 24-channel analog signal. These signals are processed by six ASD (Amplifier Shaper Discriminator) ASIC chips [22] and six ADCs (Analog Devices Inc., AD9212) before being routed to an FPGA chip (Xilinx, `Virtex-5` XC5VLX155T). The acquired data is then transmitted to a backend computer via a Small Form-factor Pluggable (SFP) slot utilizing SiTCP technology [23] through an optical fiber cable. Additionally, the board features two RJ45 connectors: one for the JTAG line, used to download firmware into the FPGA, and the other for transmitting clock, trigger, and busy signals to a custom FCT (Fast Control and Timing) board.

Modifications have been implemented on the board for the COMET experiment, primarily in two key aspects. Firstly, the ASIC chip has been replaced with a JRK B ASD CMOS chip of equivalent performance due to the obsolescence of the original chip. The PCB design was adjusted slightly to accommodate this replacement chip. Secondly, there has been a specification change in the connector for the high-speed communication port; the COMET CDC now utilizes a DisplayPort (DP) connector.

Fig. 26 displays a block diagram of the RECBE firmware, comprising five principal sections. The Fast Control block is designed to receive the reference clock and trigger (including the trigger number) from the FCT board, issuing a busy signal to halt further trigger receptions when its buffer reaches capacity. In parallel, the CDC block organizes data concerning drift time and energy deposit derived from digitized inputs by the TDC and ADC. The SiTCP block facilitates the forwarding of event data to the data-acquisition system through a Gigabit Ethernet fiber link, with TCP/IP ensuring reliable end-to-end connectivity. Configuration and status are managed via the Register block, accessible through UDP communications. Finally, the System Monitor block plays a crucial role in overseeing the board's operational status, tracking metrics such as temperature and voltage. This structure not only streamlines data processing and communication but also enhances the system's reliability and monitoring capabilities.

There are three clock domains in the RECBE, as illustrated in Fig. 26 with different colors: the yellow domain operates at 40 MHz, sourced from the FCT board; the green domain functions at 120/240 MHz, servicing the ADC with a 30 MHz clock and the TDC with a 960 MHz clock; and the blue domain runs at 125 MHz, aligned with the data transfer rate for Gigabit Ethernet. Signal and data buses crossing these clock domains are meticulously managed to prevent meta-stability issues. Due to concerns about radiation, no local clocks or nonvolatile memory are utilized within the system. It is necessary to remotely and regularly re-configure the firmware to rectify any errors induced by radiation exposure.

The ring buffer, designed to store ADC and TDC data, has a capacity of 256 depths, which equates to approximately 8.533 μs. By setting an appropriate rollback length as an offset within the ring buffer, it is possible to retrieve ADC and TDC data from about 8 μs prior. The standard event window size for the CDC is 32 samples, translating to roughly 1.067 μs. Consequently, the maximum allowable trigger latency, after accounting for the typical event window size, is about 7 μs. Additionally, as a prelude to transmission to the SiTCP module, there is a downstream buffer comprising 256-depth block RAM. Given the typical event window size, this buffer can accommodate up to 8 events.

5.2. Mass production of readout electronics

During the pre-production phase of the CDC readout electronics, four boards were assembled using lead-free solder with a peak temperature range of 245–255 °C, and another four utilized tin–lead (Sn–Pb) solder, peaking at 205–215 °C. Remarkably, only one solder joint failure was identified among the boards using Sn–Pb solder. Following assembly, a comprehensive burn-in test was conducted on these boards, which revealed no significant difference in RECBE performance between the two solder types. Based on these findings, the decision was made to opt for lead-free solder for mass production, aligning with global manufacturing standards. The durability tests conducted suggest that the RECBE's operational lifespan is projected to exceed 2.5 years, using the data garnered from this testing phase.

Mass-production of 120 readout electronics boards was efficiently completed within a span of one and a half months. This comprehensive process included soldering, assembling, functional and performance testing, followed by an aging test. A total of 126 products had successfully passed the aging test, affirming their reliability for operational use.

5.3. Radiation tolerance

Radiation damage to the front-end readout and the CDC is a critical concern for the experiment. Positioned downstream of the CDC

detector, the RECBE boards are particularly vulnerable, facing high radiation fluence from the beamline and target. To withstand such conditions, the electronics are required to endure a total radiation dose of 1.0 kGy and a neutron fluence up to 1.0×10^{12} cm^{-2}, for 1-MeV equivalent neutrons during the 150-day physics data taking period, where radiation levels include a safety factor of 5 to take into account the uncertainties in simulation results. Through rigorous irradiation testing, we have identified and selected electronic components that satisfy these stringent radiation tolerance requirements [24].

5.4. Electronics shield cover and cabling

The front-end electronics of the CDC are safeguarded by electromagnetic shield covers, strategically positioned on both the upstream and downstream end-plates. These covers are primarily constructed from 3-mm-thick aluminum plates, with their joints meticulously sealed using dismountable glue. To mitigate the risk of discharges in high-voltage components, nitrogen or dry air is circulated within these shield covers, counteracting the helium gas that fills the interior of the detector solenoid.

The installation of the 104 RECBE boards is carried out within the downstream electromagnetic shield cover. Cables extend from each board to the patch panels located on the end cap of the CyDet cradle, a cylindrical structure designed to support the CDC detector and the trigger hodoscope detector. These cables facilitate the supply of electric power, data transfer, and the distribution of clock and trigger signals, as well as the transfer of trigger data. Connections from the patch panel ensure seamless integration with each corresponding device and board positioned outside the detector solenoid.

High voltage is delivered to the CDC from the upstream side, with the high voltage cable connected to the HV module via the patch panel on the CyDet cradle. High voltage is supplied in 32 segments to ensure reliable operation under high-rate conditions, with continuous monitoring of both voltage and current. Each segment can be independently switched on or off to address any issues as safely as possible.

5.5. Cooling system

Effective heat removal from the front-end electronics within the electronics shield covers, along with precise temperature control, is crucial for the CDC detector's stable functionality. The heat generated, especially by the RECBE boards, can adversely affect electronics performance. Furthermore, maintaining a consistent temperature is vital for ensuring stable drift velocity and gas gain, which are fundamental for the gas detector's functionality. The close placement of electronics boards to the detector's downstream end-plate may lead to heat accumulation, potentially compromising the stability of gas characteristics. Therefore, meticulous temperature management within the detector is essential for sustaining optimal performance levels. Ensuring the removal of excess heat and maintaining temperature stability are paramount to prevent any detrimental effects on both the electronics and the overall detector operation.

Notably, the read-out electronics (RECBE) and specifically its FPGA component, represent the primary source of heat within the CDC detector. With 104 RECBE boards installed, the total potential heat generation is estimated to be around 2 kW. This substantial heat output necessitates a robust cooling strategy to prevent any adverse effects on the electronics' performance and, by extension, on the overall operation of the detector.

The CDC is equipped with a water cooling system, vital for maintaining the detector's operational stability. The design features cooling pipes strategically positioned on the CDC end-plate, as illustrated in Fig. 27. These pipes are placed in proximity to the RECBE boards to facilitate direct cooling of the copper blocks mounted on the FPGAs of the RECBE. With 10 circulation lines integrated into the end-plate, this configuration is engineered to provide efficient cooling, ensuring

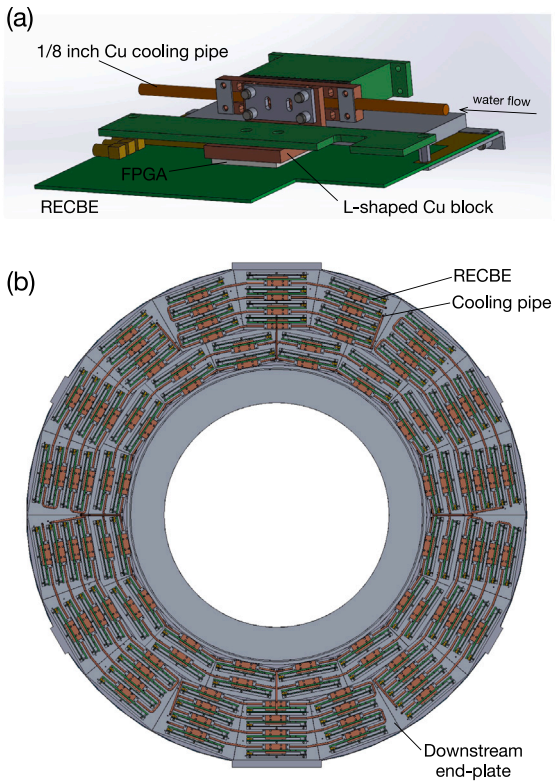

Fig. 27. The design of cooling pipes and parts on the CDC end-plate.

that the temperature of the RECBE boards remains stable. To effectively dissipate the heat generated by the system, the cooling system is designed to circulate water at a rate of approximately 3 L per minute, maintaining a 10 °C temperature differential between the inlet and outlet. To mitigate the risk of water hammer phenomena, it is crucial to maintain the flow speed below 2 meters per second and to utilize pipes with a diameter larger than 1/8 inch. Figs. 28 provide the schematic overview of the cooling system. Positioned within the experimental area, the cooling system includes the water pipes within the radiation-controlled zone. The water is collected in a 100-L buffer tank, equipped with a sampling port for conducting activity measurements. Ensuring efficient operation, the water-cooling apparatus is designed for high pumping speed and cooling power, with remote controllability for added convenience. Additionally, a corrosion prevention material is applied to the pipes to safeguard against corrosion.

In environments with high humidity, the cooling process may lead to condensation, posing a risk to sensitive electronic components. To counteract this potential threat, it is essential to introduce a continuous flow of nitrogen or dry air within the electronics cover. This measure effectively reduces the humidity level inside, safeguarding the electronics from moisture-related damage. Additionally, the infusion of nitrogen or dry air plays a critical role in preventing electrical discharges at high-voltage pins, further enhancing the system's operational safety and reliability. By maintaining a controlled, low-humidity environment around the electronics, this approach ensures the integrity and longevity of the components, particularly in the context of cooling systems that could otherwise introduce moisture through condensation.

6. Cosmic-ray tests

Performance tests for the CDC have been conducted using cosmic-rays without a magnetic field [25,26]. Fig. 29 shows a cosmic ray test setup for the CDC. For these tests, the detector was operated stably

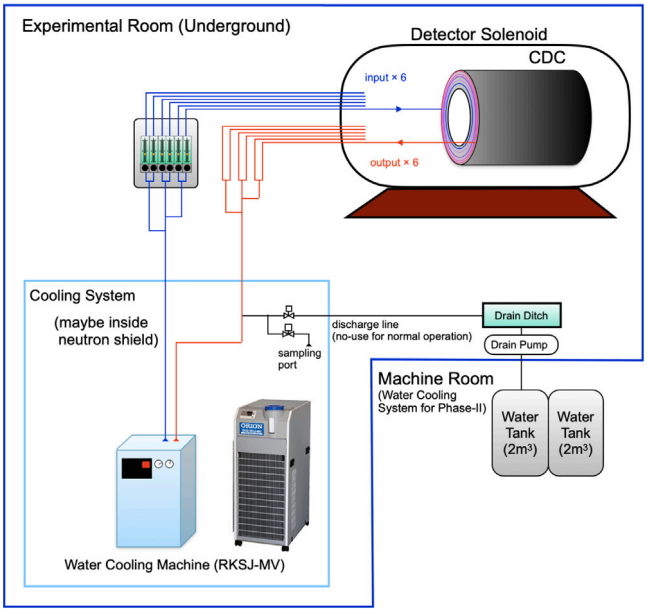

Fig. 28. Diagram of the water cooling system for the CDC electronics.

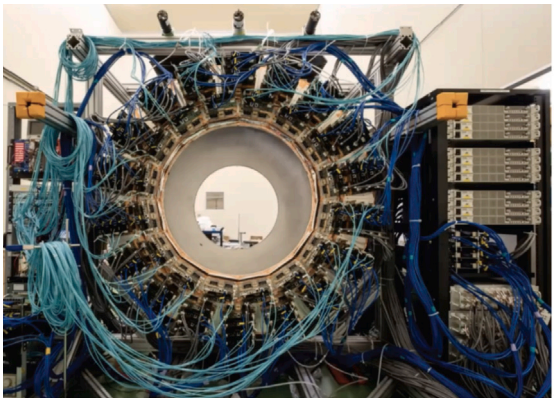

Fig. 29. Photograph of the CDC cosmic-ray test setup.

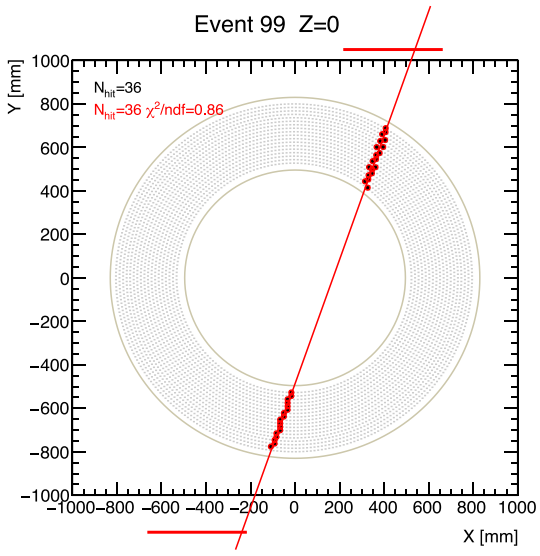

Fig. 30. Typical event display of cosmic-ray events as observed at the CDC's central plane. Black dots and red circles trace the trajectory of a cosmic-ray track, where the black dots represent the locations of hit wires, and the red circles illustrate the corresponding drift circles. Additionally, red bars positioned outside the main plot delineate the locations of trigger counters.

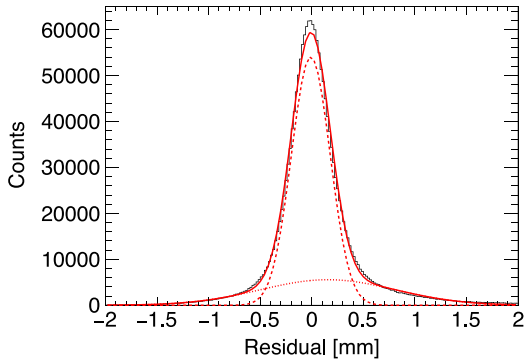

Fig. 31. Residual distribution for a central layer at +1850 V, fitted with a double Gaussian function.

with a gas mixture of He:i-C_4H_{10} (90:10), under high voltages reaching up to +1850 V. The data acquisition system functioned effectively, seamlessly integrating with all 104 RECBE boards and the trigger system as detailed in Section 5.

We developed a straight track reconstruction program tailored for the all-stereo drift chamber, based on methodologies outlined in [27]. Fig. 30 presents a typical event display, featuring a clearly discernible cosmic-ray track. For subsequent analysis, we used reconstructed tracks with a good χ^2 value and containing a sufficiently large number of hits (i.e., larger than 10 and 33 in position resolution and efficiency analyses, respectively). .

Fig. 31 illustrates a typical residual distribution, calculated from the difference between the drift distance and the closest approach distance of a hit wire to a reconstructed track. Importantly, the hit under examination was omitted from the tracking analysis. This residual distribution was modeled using a double Gaussian function, revealing a core part with a standard deviation of 180 μm including tracking uncertainty. The distribution's tail portion can be attributed to two main factors: firstly, the generation of a relatively small number of primary electron–ion pairs within a cell, a trait commonly associated with helium-based gas mixtures; and secondly, distortions in the electric field near the cell edges.

The overall position resolution was found to be within the range of 170–190 μm. Fig. 32 depicts the position resolution as a function of the distance from a sense wire, illustrating how resolution varies across different regions of the cell. Notably, the resolution remains below 150 μm within the central range but increases in proximity to both the sense and field wires. This variation is due to multiple factors: at shorter distances, the resolution is compromised by the scarce production of primary electrons, whereas at longer distances, it is influenced by the longitudinal diffusion of electrons. Additionally, near the cell edges, distortion of the electric field emerges as a significant factor degrading resolution.

Hit efficiency for a single cell was assessed using tracks reconstructed without incorporating a hit from the cell under examination. This efficiency is quantified as the ratio of detected hits in a cell to the total number of tracks traversing it. Fig. 33 illustrates hit efficiency relative to the distance from a sense wire, categorized into three distinct levels based on hardware or software criteria. Hardware hit efficiency encompasses all detected hits within TDC data, while software hit efficiency mandates a favorable residual of drift distance. Specifically, 5σ and 3σ software efficiencies necessitate residuals within five and three standard deviations of the residual distribution, respectively. These software efficiencies are considered to be used in the track fitting

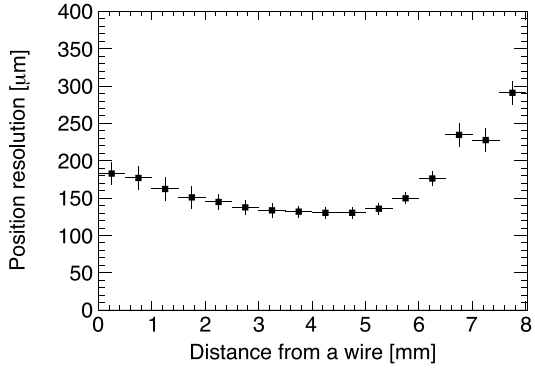

Fig. 32. Position resolution as a function of distance from a sense wire in a central layer at +1850 V.

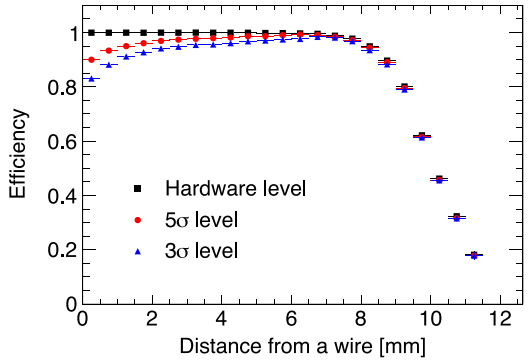

Fig. 33. Hit efficiency as a function of distance from a sense wire in a central layer at +1800 V. The black squares indicate hardware efficiency, and the red circles and blue triangles represent software efficiencies defined within 5σ and 3σ ranges in the residual, respectively.

process. An almost 100% hardware efficiency was achieved across the standard cell size of 8 mm. Conversely, software efficiencies tend to decrease at shorter drift distances due to the deterioration of position resolution near the wire. Distances exceeding 8 mm usually indicate cell corners, where tracks cross only part of the cell; such cases are expected to be compensated by adjacent cells.

7. Operational environment of CDC

This section describes the operational environment of the CDC during the 150-day COMET Phase-I physics measurements.

In the Phase-I experiment, a pulsed muon beam is generated by bombarding a carbon target with an 8 GeV, 3.2 kW pulsed proton beam, derived from the slow extraction process of the J-PARC main ring. The proton beam pulse is approximately 100 ns wide, with a beam spacing during extraction of 1.17 μs. The beam duty factor of the main ring can range from 3 to 5. At the entrance to the CyDet, the average muon rate reaches 1.3×10^{10} Hz with 9.4% of these muons stopping at the muon stopping targets, resulting in a muon stop rate of about 1.2×10^{9} Hz. Secondary and tertiary particles, produced by stopped muons and pions within and around the stopping targets, are subsequently injected into the CDC region. In addition, beam flash particles, which consist mainly of electrons and gamma rays, arrive in large numbers immediately after the beam pulse timing and are also a significant factor in determining the radiation environment of the CDC.

To assess the impact of these particles on the CDC, Monte Carlo simulations were utilized to compute the cell hit rate and the accumulated charge on each wire [2]. In this study, the simulation did not include the contribution of long-duration backgrounds. The results

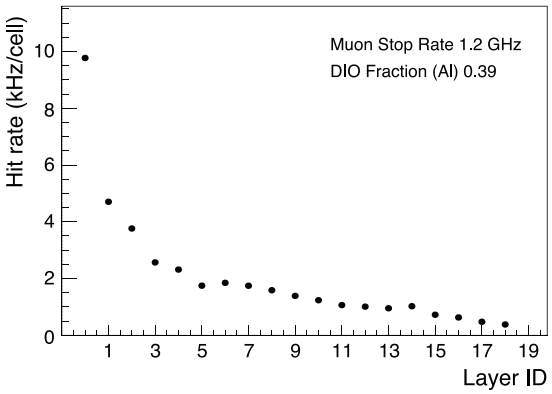

Fig. 34. DIO electron hit rate for each CDC cell layer. Layer ID 1 is the innermost sense layer.

suggest that the influence of neutrons within the detector vicinity is minimal, supporting the feasibility of achieving the experimental objectives under the expected conditions.

7.1. Hit rate

Stopped muon-induced particles are the primary contributors to the increased hit rate observed in the CDC. Among the secondary particles, the DIO (decay-in-orbit) electrons are of particular concern and must be carefully considered. Fig. 34 presents the evaluated DIO-induced hit rates for each cell layer within the CDC. To minimize the impact of DIO electron hits, the innermost layer of the CDC was designed with a sufficiently large installation radius. DIO electrons that interact with the CDC typically originate from either the high-energy tail of the DIO spectrum or from muons stopped in regions such as the helium gas near the inner wall. As a result, the hit rate in the CDC decreases significantly from the innermost to the outermost layers. The time-averaged hit rate for the innermost sense wire is estimated to be a maximum of 5 kHz/cell. Given that the duty factor of the proton beam cycle from the J-PARC main ring is assumed to be 3, the corresponding instantaneous hit rate is around 15.6 kHz/cell. Consequently, the hit occupancy for the innermost layer, during a bunch cycle of 1.17 μs, is approximately 1.8%. Some of the particles generated from the muon capture process also contribute to hits in the CDC. The time-averaged hit rate attributed to protons emitted from excited nuclei was evaluated to be 1.4 kHz/cell. Taking into account other hit sources after nuclear muon capture, such as bremsstrahlung photons, muonic X-rays, neutrons, and γ-rays from excited nuclei, the hit occupancy in the CDC due to stopped muons was calculated to be between 7% and 10%. This result is depicted by the magenta dots in Fig. 35. Additionally, the contribution to the hit rate from stopped pions is represented by the cyan dots in the same figure. Compared to the other categories, the contribution from stopped pions is relatively small.

The first few tens of nanoseconds of the pulsed beam, which reaches the detector area every 1.17 μs, generates a high-intensity beam flash composed primarily of electrons, γ-rays, and neutrons. Although the beam flash itself is brief, it significantly impacts the hit occupancy rate due to the CDC cell's maximum drift time of approximately 700 ns. As illustrated by the blue dots in Fig. 35, the contribution of beam flashes to hit occupancy is estimated to be around 4% across all layers.

When considering all contributing factors, the overall hit occupancy was evaluated to be 15% for the innermost layer and 11% for the outermost layer, as shown in Fig. 35. To efficiently select hits corresponding to signal events within this high hit occupancy data, analysis programs are being developed that leverage the charge information of each cell and utilize hit pattern selection techniques through machine learning.

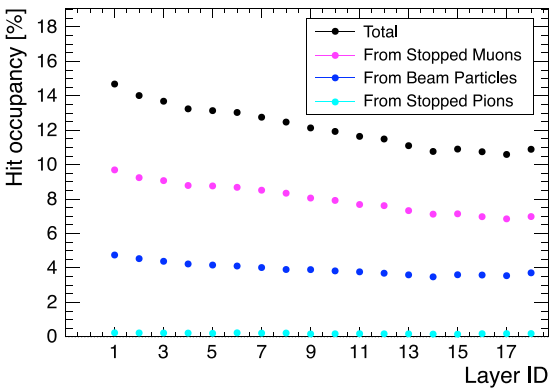

Fig. 35. CDC single hit occupancy as a function of the CDC layers with the assumption of a beam duty factor of 3.

7.2. Accumulated charge

The lifetime-accumulated charge on a wire is a critical factor in predicting performance degradation due to wire aging. As previously mentioned, CDC cells are subjected to high hit rates. However, the most significant contributor to wire aging is the effect of low-energy protons and light ions emitted during the muon nuclear capture process and other similar processes. These particles result in localized energy deposits that are approximately 100 times greater than those from minimum ionizing particles. Geant4 simulations have been used to investigate the charge accumulation rates, which were found to be 0.09 mC/cm/day/wire for the innermost sense layer and 0.05 mC/cm/day/wire for the outermost sense layer. Consequently, the maximum accumulated charge by the end of the 150 days of COMET Phase-I operation is projected to be 14 mC/cm/wire.

To investigate the effects of aging, measurements were conducted using a small drift chamber. This chamber consisted of nine cells surrounded by guard wires, and it was constructed using wires and feedthroughs similar to those employed in the actual CDC, with silicone rubber used to secure them to the end plates. A single wire within this setup was irradiated with beta radiation from a ^{90}Sr source, at a charge accumulation rate approximately 130 times that expected in the COMET experiment. Preliminary results indicated that when the He:i-C_4H_{10} (90:10) gas mixture was combined with around 1100–1300 ppm of water, the gain reduction rate was 1.7% at 20 mC/cm/wire and approximately 6% at 200 mC/cm/wire [28]. In a study of KEK-Belle's CDC, which also uses silicone rubber for securing feedthroughs, similar to the COMET CDC, the gain degradation rate was reported to be less than 1% even at an accumulated charge of 150 mC/cm/wire for the He:C_2H_6 (50:50) gas mixture in an aging test conducted one year after production [29].

8. Conclusion

The CDC for the COMET Phase-I experiment, which is aiming at detecting the charged lepton flavor violating $\mu \to e$ conversion process with a remarkable single event sensitivity of 3×10^{-15} at J-PARC, has been designed and constructed. Designed for optimal performance, the CDC can efficiently measure 104.9 MeV/c signal electrons while effectively suppressing unwanted background events.

To achieve the necessary momentum resolution of 200 keV/c, the CDC operates with a low-Z gas mixture of He:i-C_4H_{10} (90:10) to mitigate the multiple scattering effect. Its configuration of all-stereo layers is specifically designed to improve position resolution in the longitudinal direction. The CDC comprises 4,986 sense wires made of gold-plated tungsten and 14,562 field wires crafted from aluminum.

Initial cosmic-ray tests for the CDC have demonstrated commendable performance, achieving expected hit efficiency and position resolution. These results validate the robustness of the CDC design and its capability to meet the stringent requirements of the COMET Phase-I experiment.

CRediT authorship contribution statement

A. Sato: Writing – review & editing, Writing – original draft, Visualization, Validation, Supervision, Software, Project administration, Investigation, Conceptualization. **H. Yoshida:** Writing – review & editing, Writing – original draft, Visualization, Supervision, Software, Investigation, Data curation. **M. Moritsu:** Writing – review & editing, Writing – original draft, Visualization, Validation, Supervision, Software, Investigation, Data curation. **X. Jiang:** Supervision, Project administration, Methodology, Investigation. **Y. Kuno:** Writing – review & editing, Writing – original draft, Supervision, Project administration, Investigation, Funding acquisition, Conceptualization. **H.-B. Li:** Supervision, Project administration, Funding acquisition. **W.-G. Li:** Supervision, Project administration. **Y. Matsuda:** Software, Investigation. **H. Miao:** Software, Investigation. **Y. Nakamura:** Software, Investigation. **Y. Nakatsugawa:** Software, Investigation. **Y. Nakazawa:** Writing – review & editing, Software, Investigation. **S. Ohta:** Software, Investigation. **K. Okinaka:** Software, Investigation. **H. Sakamoto:** Software, Investigation. **M.L. Wong:** Software, Investigation. **T.S. Wong:** Software, Investigation. **C. Wu:** Writing – review & editing, Writing – original draft, Visualization, Software, Investigation. **T.-Y. Xing:** Software, Investigation. **T. Yamane:** Software, Investigation. **Y. Yuan:** Supervision, Software, Project administration, Investigation. **J. Zhang:** Software, Investigation. **Y. Zhang:** Supervision, Software, Project administration, Investigation, Funding acquisition, Data curation. **Z.-K. Zhang:** Software, Investigation.

Declaration of competing interest

The authors declare that they have no known competing financial interests or personal relationships that could have appeared to influence the work reported in this paper.

Data availability

Data will be made available on request.

Acknowledgments

We extend our deepest appreciation to Prof. S. Uno and Prof. T. Koriki from KEK for their invaluable advice and steadfast support throughout the design, construction, and operational phases of the CDC. We are also profoundly grateful to all of COMET collaborators and members of Hayashi-Repic Co., Ltd. for their indispensable assistance in the construction of the CDC, particularly in the meticulous process of wire stringing.

This work was supported by the Japan Society for the Promotion of Science (JSPS) KAKENHI, under Grant Numbers JP25000004 and JP18H05231, as well as a Grant-in-Aid for JSPS Fellows, Japan, JP17J07754. Additional support was provided by the Beijing Natural Science Foundation, China (International Scientists Project) No. IS23012; the International Partnership Program of the Chinese Academy of Sciences, Grant No. 113111KYSB20190035; and the National Natural Science Foundation of China (NSFC) under Contract No. 11335009 and No. 11475208.

References

[1] Y. Kuno, Y. Okada, Muon decay and physics beyond the standard model, Rev. Modern Phys. 73 (2001) 151–202, http://dx.doi.org/10.1103/RevModPhys.73.151, arXiv:hep-ph/9909265.

[2] R. Abramishvili, et al., COMET phase-I technical design report, PTEP 2020 (3) (2020) 033C01, http://dx.doi.org/10.1093/ptep/ptz125, arXiv:1812.09018.

[3] W.H. Bertl, et al., A search for muon to electron conversion in muonic gold, Eur. Phys. J. C47 (2006) 337–346, http://dx.doi.org/10.1140/epjc/s2006-02582-x.

[4] C. Hoppner, S. Neubert, B. Ketzer, S. Paul, A novel generic framework for track fitting in complex detector systems, Nucl. Instrum. Methods Phys. Res. A 620 (2) (2010) 518–525, http://dx.doi.org/10.1016/j.nima.2010.03.136, URL https://www.sciencedirect.com/science/article/pii/S0168900210007473.

[5] M. Adinolfi, et al., The tracking detector of the KLOE experiment, Nucl. Instrum. Methods Phys. Res. A 488 (1) (2002) 51–73, http://dx.doi.org/10.1016/S0168-9002(02)00514-4, URL https://www.sciencedirect.com/science/article/pii/S0168900202005144.

[6] S. Uno, Y. Sakai, T. Tsukamoto, K. Abe, I. Adachi, T. Nozaki, M. Saitoh, O. Sasaki, H. Yamaoka, K. Emi, O. Nitoh, K. Takahashi, M. Aoki, R. Kajikawa, K. Miyabayashi, E. Nakano, Y. Ohnishi, K. Shimozawa, A. Sugiyama, S. Suzuki, F. Teramae, T. Toyama, T. Yamaki, Study of a drift chamber filled with a helium-ethane mixture, Nucl. Instrum. Methods Phys. Res. A 330 (1) (1993) 55–63, http://dx.doi.org/10.1016/0168-9002(93)91304-6, URL https://www.sciencedirect.com/science/article/pii/0168900293913046.

[7] J.A. Kadyk, Wire chamber aging, Nucl. Instrum. Methods Phys. Res. A 300 (3) (1991) 436–479, http://dx.doi.org/10.1016/0168-9002(91)90381-Y, URL https://www.sciencedirect.com/science/article/pii/016890029190381Y.

[8] R. Veenhof, Simulation of gaseous detectors, URL http://garfield.web.cern.ch/garfield.

[9] C. Wu, T. Wong, Y. Kuno, M. Moritsu, Y. Nakazawa, A. Sato, H. Sakamoto, N. Tran, M. Wong, H. Yoshida, T. Yamane, J. Zhang, Test of a small prototype of the COMET cylindrical drift chamber, Nucl. Instrum. Methods Phys. Res. A 1015 (2021) 165756, http://dx.doi.org/10.1016/j.nima.2021.165756, URL https://www.sciencedirect.com/science/article/pii/S0168900221007415.

[10] A. Baldini, E. Baracchini, C. Bemporad, et al., The design of the MEG II experiment, Eur. Phys. J. C 78 (2018) 380, http://dx.doi.org/10.1140/epjc/s10052-018-5845-6.

[11] A.M. Baldini, et al., Performances of a new generation tracking detector: the MEG II cylindrical drift chamber, Eur. Phys. J. C 84 (5) (2024) 473, http://dx.doi.org/10.1140/epjc/s10052-024-12711-y, arXiv:2310.12865.

[12] A. Sharma, F. Sauli, Low mass gas mixtures for drift chambers operation, Nucl. Instrum. Methods Phys. Res. A 350 (3) (1994) 470–477, http://dx.doi.org/10.1016/0168-9002(94)91246-7, URL https://www.sciencedirect.com/science/article/pii/0168900294912467.

[13] S. Navas, et al., Review of particle physics, Phys. Rev. D 110 (2024) 030001, http://dx.doi.org/10.1103/PhysRevD.110.030001, URL https://link.aps.org/doi/10.1103/PhysRevD.110.030001.

[14] F. Sauli, Principles of operation of multiwire proportional and drift chambers, 1977, CERN-77-07.

[15] A. Gaponenko, A. Grossheim, A. Hillairet, G.M. Marshall, R.E. Mischke, A. Olin, Charged-particle spectra from μ^- capture on al, Phys. Rev. C 101 (2020) 035502, http://dx.doi.org/10.1103/PhysRevC.101.035502, URL https://link.aps.org/doi/10.1103/PhysRevC.101.035502.

[16] A. Edmonds, J. Quirk, M.-L. Wong, D. Alexander, R.H. Bernstein, A. Daniel, E. Diociaiuti, R. Donghia, E.L. Gillies, E.V. Hungerford, P. Kammel, B.E. Krikler, Y. Kuno, M. Lancaster, R.P. Litchfield, J.P. Miller, A. Palladino, J. Repond, A. Sato, I. Sarra, S.R. Soleti, V. Tishchenko, N.H. Tran, Y. Uchida, P. Winter, C. Wu, Measurement of proton, deuteron, triton, and α particle emission after nuclear muon capture on Al, Si, and Ti with the AlCap experiment, Phys. Rev. C 105 (2022) 035501, http://dx.doi.org/10.1103/PhysRevC.105.035501, URL https://link.aps.org/doi/10.1103/PhysRevC.105.035501.

[17] T. Abe, et al., Belle II technical design report, 2010, arXiv:1011.0352.

[18] W. Blum, W. Riegler, L. Rolandi, Particle Detection with Drift Chambers, Springer-Verlag, Berlin Heidelberg, 2008, http://dx.doi.org/10.1007/978-3-540-76684-1, URL https://link.springer.com/book/10.1007/978-3-540-76684-1.

[19] N. Taniguchi, Central drift chamber for Belle-II, J. Instrum. 12 (06) (2017) C06014, http://dx.doi.org/10.1088/1748-0221/12/06/C06014.

[20] N. Taniguchi, M. Ikeno, Y. Iwasaki, M. Saito, S. Shimazaki, M. Tanaka, T. Uchida, S. Uno, All-in-one readout electronics for the Belle-II central drift chamber, Nucl. Instrum. Methods Phys. Res. A 732 (2013) 540–542, http://dx.doi.org/10.1016/j.nima.2013.06.096, Vienna Conference on Instrumentation 2013, URL https://www.sciencedirect.com/science/article/pii/S0168900213009509.

[21] T. Uchida, M. Ikeno, Y. Iwasaki, M. Saito, S. Shimazaki, M. Tanaka, N. Taniguchi, S. Uno, Readout electronics for the central drift chamber of the Belle II detector, in: 2011 IEEE Nuclear Science Symposium Conference Record, 2011, pp. 694–698, http://dx.doi.org/10.1109/NSSMIC.2011.6154084.

[22] S. Shimazaki, T. Taniguchi, T. Uchida, M. Ikeno, N. Taniguchi, M.M. Tanaka, Front-end electronics of the Belle II drift chamber, Nucl. Instrum. Methods Phys. Res. A 735 (2014) 193–197, http://dx.doi.org/10.1016/j.nima.2013.09.050, URL https://www.sciencedirect.com/science/article/pii/S0168900213012849.

[23] T. Uchida, Hardware-based TCP processor for gigabit ethernet, IEEE Trans. Nucl. Sci. 55 (2008) 1631–1637, application/pdf.

[24] Y. Nakazawa, et al., Radiation hardness study for the COMET Phase-I electronics, Nucl. Instrum. Methods A 955 (2020) 163247, http://dx.doi.org/10.1016/j.nima.2019.163247, arXiv:1912.01742.

[25] M. Moritsu, Y. Kuno, Y. Matsuda, Y. Nakazawa, K. Okinaka, H. Sakamoto, A. Sato, M. Wong, T. Wong, C. Wu, T. Yamane, H. Yoshida, H. Li, J. Xiaoshan, J. Zhang, Construction and performance tests of the COMET CDC, Proc. Sci. 340 (2019) 538, http://dx.doi.org/10.22323/1.340.0538.

[26] M. Moritsu, Y. Kuno, Y. Matsuda, Y. Nakazawa, S. Ohta, H. Sakamoto, A. Sato, M. Wong, T. Wong, C. Wu, H. Yoshida, X. Jiang, H. Li, J. Zhang, Commissioning of the cylindrical drift chamber for the COMET experiment, Proc. Sci. 364 (2020) 128, http://dx.doi.org/10.22323/1.364.0128.

[27] G. Cataldi, V. Elia, E. Gorini, F. Grancagnolo, M. Primavera, S. Spagnolo, Straight tracks reconstruction in all stereo drift chambers, Nucl. Instrum. Methods Phys. Res. A 388 (1) (1997) 127–134, http://dx.doi.org/10.1016/S0168-9002(97)00306-9, URL https://www.sciencedirect.com/science/article/pii/S0168900297003069.

[28] Y. Nakamura, Wire Aging Tests for COMET CDC (in Japanese) (Master's thesis), Graduate School of Science, Osaka University, 2018.

[29] S. Uno, Drift chamber for super-belle, 2003, Slide of the Super B-factory Workshop in Hawai.